ARTICLE OPEN

Check for updates

Stochastic resonance in 2D materials based memristors

J. B. Roldán [1] ✉, A. Cantudo[1], J. J. Torres [2], D. Maldonado [1,3], Yaqing Shen[4], Wenwen Zheng[4], Yue Yuan[4] and M. Lanza [4] ✉

Stochastic resonance is an essential phenomenon in neurobiology, it is connected to the constructive role of noise in the signals that take place in neuronal tissues, facilitating information communication, memory, etc. Memristive devices are known to be the cornerstone of hardware neuromorphic applications since they correctly mimic biological synapses in many different facets, such as short/long-term plasticity, spike-timing-dependent plasticity, pair-pulse facilitation, etc. Different types of neural networks can be built with circuit architectures based on memristive devices (mostly spiking neural networks and artificial neural networks). In this context, stochastic resonance is a critical issue to analyze in the memristive devices that will allow the fabrication of neuromorphic circuits. We do so here with h-BN based memristive devices from different perspectives. It is found that the devices we have fabricated and measured clearly show stochastic resonance behaviour. Consequently, neuromorphic applications can be developed to account for this effect, that describes a key issue in neurobiology with strong computational implications.

INTRODUCTION

Stochastic resonance (SR) includes phenomena linked to the constructive effect of noise, e.g., a signal that is normally too weak to be detected by a sensor can be partially detected by adding noise (see Fig. 1). SR was first proposed in 1980 by Benzi et al. [1] using numerical methods, and later studies applied the concept of SR in a wide variety of research fields, such as medical care[2] and biology[3,4]. Within this last one, SR is particularly useful for sensory neurobiology, and it has been employed for explaining the animal behaviours that lead to evolutionary success[3–8]. For example, paddlefishes use SR to detect food with their rostrum (an optimal amount of noise allows them to capture more plankton from their surroundings)[9], and crickets use SR to escape from predator wasps[10]. The reason is that the building blocks of biological brains (i.e., the neurons and the synapses) produce electrical signals whose features can be described via SR[3,4].

It is then not a surprise that recently SR has also started to attract attention in the field of brain-inspired computing and neuromorphic engineering. As in its biological counterparts, electronic neurons and synapses store and compute data by producing electronic signals (mainly trains of spikes), in which electrical noise can bring associated constructive effects leading to SR[11]. However, realizing solid-state micro/nano-electronic devices for the hardware implementation of electronic neurons and synapses exhibiting SR can be challenging. SR has been observed in Schmitt triggers[12], tunnel diodes[13], phase change materials in networked nonlinear systems[7,8,14,15], and different types of photodetectors[16]. In these devices the concept of resonance is connected to a maximum signal-to-noise ratio or an optimal noise frequency that produces a better output response than without the noise or with noise of other frequencies.

Recently, memristors showing high nonlinearity have been proposed for the hardware implementation of electronic neurons and synapses[17]. In brief, memristors consist of an ultra-thin insulating film with two or three adjacent metallic electrodes, and the resistance of the insulator can be adjusted to different levels

by applying electrical stresses to the electrodes[18–21]. In these devices, the concept of SR comes up in a natural manner because there are many parameters capable of performing the thresholding operation, such as the intensity and duration of the electrical stresses applied (either voltage or current)[11]. The competitive advantage of nonlinear memristors over the rest of aforementioned devices for the hardware implementation of electronic neurons and synapses with SR is the coherent implementation of spike generation mechanisms accounting for thresholding. Moreover, they can also show non-volatile multilevel operation that is essential for synaptic weight building in artificial neural networks. However, nonlinear memristors made of traditional materials (metal-oxides, phase-change materials) suffer from variability[22,23] and reliability issues[18,24], and intense research on other potential candidate memristive materials, devices and systems is necessary.

Here we show the fabrication, characterization and modeling of memristors with metal/h-BN/metal structure, in which hexagonal boron nitride (h-BN) is a two-dimensional (2D) layered material with insulating properties (band gap ~5.9 eV, dielectric constant ~3). We introduce different types of electrical noise (Gaussian, exponential) in the biasing signals applied to the devices, and we clearly observe the presence of the SR phenomenon by analysing the state transitions. We show SR effects by using two different approaches to detect and measure this phenomenon.

RESULTS AND DISCUSSION

Device fabrication

We fabricated and measured our h-BN based memristors using only methods scalable to the wafer level, ensuring compatibility with the industry standards, as described in the methods section. In particular, chemical vapour deposition (CVD) was used to synthesize the h-BN stack, which was placed between two metallic electrodes made of Au (40 nm) on Ti (10 nm), see Fig. 2a. The lateral size of the cross-point Au/Ti/h-BN/Au memristors was 5 μm × 5 μm, see Fig. 2c and h. This type of structures are known to exhibit stable

[1]Departamento de Electrónica y Tecnología de Computadores. Universidad de Granada. Facultad de Ciencias. Avenida Fuentenueva s/n, 18071 Granada, Spain. [2]Institute "Carlos I" for Theoretical and Computational Physics and Department of Electromagnetism and Matter Physics, University of Granada, 18071 Granada, Spain. [3]IHP-Leibniz-Institut fuer innovative Mikroelektronik, 15236 Frankfurt (Oder), Germany. [4]Materials Science and Engineering Program, Physical Sciences and Engineering Division, King Abdullah University of Science and Technology (KAUST), Thuwal 23955-6900, Saudi Arabia. ✉email: jroldan@ugr.es; mario.lanza@kaust.edu.sa

non-volatile bipolar resistive switching (RS) behaviour, which has been demonstrated by several independent groups[25–27].

Electrical characterization of memristive effects

We applied sequences of ramped voltage stresses (RVS) with different polarities to the top Au/Ti electrode of fresh memristors (Fig. 2d), keeping the bottom electrode grounded. Initially the devices exhibit high resistances running from 10^3 to 10^4 MΩ (read at 0.1 V), and the currents driven by the Au/Ti/h-BN/Au devices stay below 1 μA for voltages up to 2 V. If the voltage is increased,
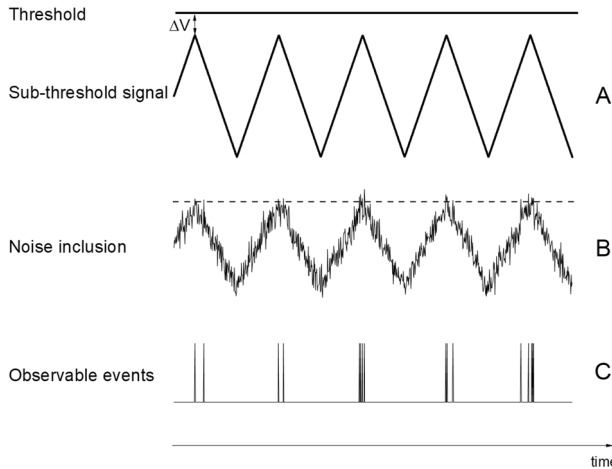
Fig. 1 Schematic of stochastic resonance effects. A It describes that a subthreshold input signal does not produce any output at all because of the nature of the system (in order to get an output, the input signal has to overpass the threshold). In our case, the existence of set and reset voltages and the difference between these internal device parameters and the input signals are responsible for the thresholding (the inherent device variability has to be taken in to consideration[22]). **B** The addition of noise to the original subthreshold input signal makes the total input signal (the sum of both signals) cross the threshold and generate some spikes as output signal, see (**C**). The constructive role of the added noise is therefore easily seen.

the current across the devices increases sharply, leading to resistances of 45 Ω (read at 0.1 V). If the bias is switched off, the resistance value persists over time, indicating the resistance change is a non-volatile effect. After that, if a RVS with negative polarity is applied, the resistance of the h-BN stack suddenly increases to values running from 1 to 10^3 MΩ (read at 0.1 V); this transition, takes place at voltages between −0.5 and −1 V (Fig. 2e). Then, if another positive RVS is applied, the device resistance decreases sharply to values that are similar to those reached after the first RVS (Fig. 2f). Figure 2b shows a cross-sectional transmission electron microscope (TEM) image of the CVD-grown multilayer h-BN stack; a the top-view optical microscope image of some metal/h-BN/metal devices is also shown (Fig. 2c), and the current versus voltage (I-V) plots recorded during the three types of RVS, showing clear the abrupt resistance changes (Fig. 2d–f). Notice that in the case of exfoliated h-BN (Fig. 2g) the devices do not show resistive switching (Fig. 2i).

After that, if more sequences of RVS with alternating polarities are applied, one can switch the device systematically between two non-volatile resistance states, namely high resistive state (HRS) and low resistance state (LRS). This phenomenon is known as non-volatile bipolar resistive switching (RS), and it has been observed in different materials including phase-change materials, metal-oxides, magnetic materials, ferroelectric materials, organic materials and 2D materials (among others)[28]. This effect is already being used in commercially available electronic memories, and it might be also useful for data computation, encryption and transmission[18]. The transition from HRS to LRS is often referred to as the set process, and the transition from LRS to HRS is often referred to as the reset process. Note that the device resistance, when it is fresh, is even higher than in HRS, and that the sudden sharp increase of current during the first positive RVS takes place at voltages that are significantly higher than in the next positive RVS. That is why the first transition is normally distinguished from the rest and it is named the forming process. However, as shown in Fig. 2e and f, corresponding to set and reset plots, the resistance achieved after the reset is much lower than when it is fresh, and for that reason the forming process does not play an important role in the normal device operation (although it must be considered when programming the devices for the first time).
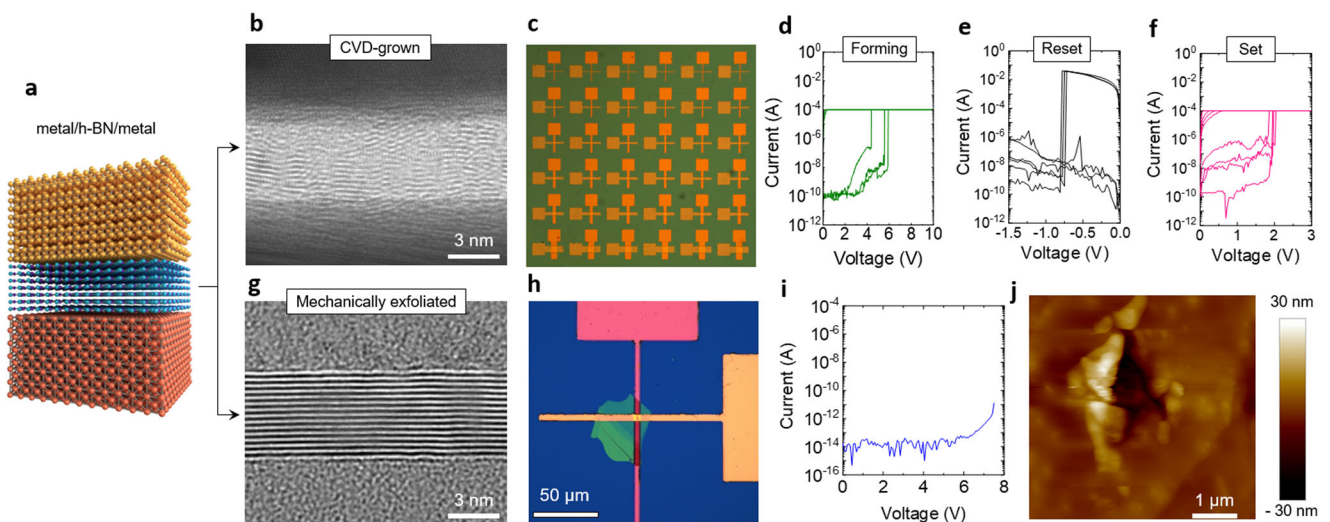

Fig. 2 Electrical phenomena in CVD-grown and mechanically exfoliated h-BN. a Three-dimensional schematic of a metal/h-BN/metal structure. **b** Cross-sectional TEM image of the multilayer CVD-grown h-BN stack, **c** top view optical microscope image of an array of metal/h-BN/metal memristors. **d** Forming plots of several Au/Ti/h-BN/Au devices, and the (**e**) reset and (**f**) set plots showing a few non-volatile bipolar RS in a single device. **g** Cross-sectional TEM image of the multilayer mechanically exfoliated h-BN stack, **h** top view optical microscope image of a metal/h-BN/metal memristor, **i** forming plot of the device corresponding to (**g**), and **j** topographic AFM map after the spot showing irreversible breakdown by material removal (i.e., crater formation).
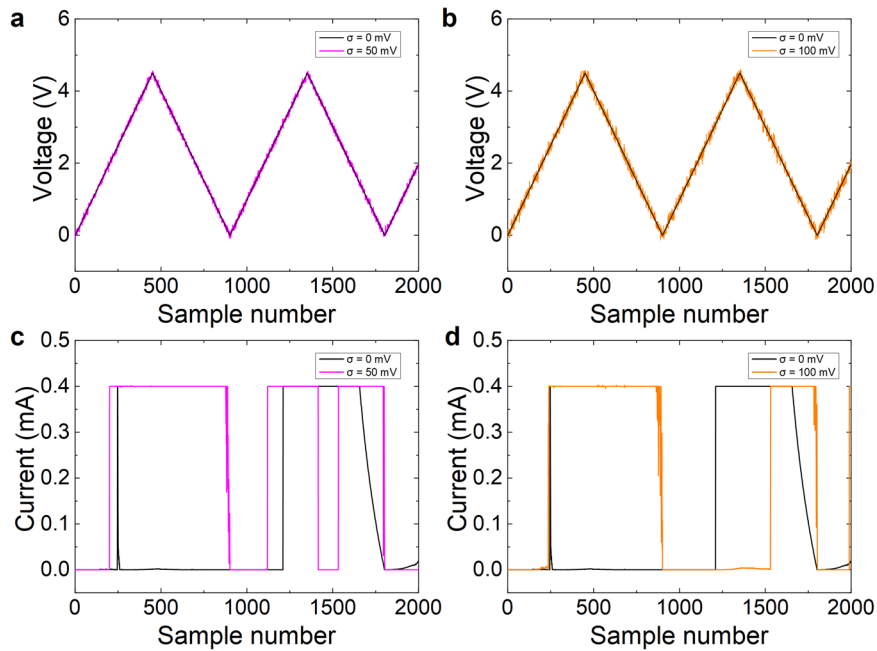
Fig. 3 Input signals with added noise. Input voltage signal versus sample number without noise and with added Gaussian noise for two different standard deviations, **a** $\sigma = 50$ mV, **b** $\sigma = 100$ mV. Corresponding measured current for an input signal without noise and with Gaussian noise for the same noise intensities employed in (**a**) and (**b**) (**c** $\sigma = 50$ mV, **d** $\sigma = 100$ mV).

The non-volatile bipolar filamentary resistive switching mechanism[25,29] is facilitated by the creation and rupture of one or a few conductive nanofilaments (CNFs) during the SET and RESET state transitions. The RS operation in our devices is linked to Ti^{X+} ions dynamics. For positive voltages, Ti^{X+} ions move toward the cathode across the dielectric[30]. This process helps in the CNF formation across the h-BN multilayer, short-circuiting the electrodes. Ti^{X+} ions are assumed to diffuse in regions with lower density of the material and large density of B and N vacancies, that favour their migration. For negative bias (the bottom electrode is always grounded) Ti^{X+} ions may diffuse back to their original positions leading to the CNF rupture and the consequent reset process[25,31,32]. The polycrystalline h-BN grown by CVD allows RS operation because it includes insulating 2D layered regions as well as defect clusters that are more conducting (defect clusters may be linked to lattice distortions that propagate from one layer to another[29,31]). Other types of h-BN, such as exfoliated h-BN (Fig. 2g), do not exhibit RS[33]. The reason is clear, in exfoliated h-BN there are no regions with high density of defects to facilitate the diffusion of Ti^{X+} ions that lead to the CNF formation. See the current versus voltage plot in this type of devices (Fig. 2i), no resistance change is seen even at high voltages.

The very sharp current decrease during the RESET transition indicates that the filament disruption is due to the Joule effect (Fig. 2e), caused by the high currents flowing through the filament, which are around 10 mA and in some cycles they can reach ~100 mA. This increases the local temperature of the filaments until they melt[34,35].

In the Au/Ti/h-BN/Au devices fabricated using CVD-grown multilayer h-BN, the value of the resistance in HRS (namely, R_{HRS}) and LRS (R_{LRS}) reasonably maintains its value from one cycle to another. The changes are due to the inherent stochasticity of the atomic rearrangements involved in the formation and disruption of the conductive nanofilament. The resistance values in each state, measured at a read voltage (V_{READ}) of 0.1 V, are roughly $R_{HRS} \sim 575.5$ MΩ and $R_{LRS} \sim 156.7$ Ω, and the R_{HRS}/R_{LRS} ratio is always above 1000; this is large enough to warrant easy state detection in each cycle for 100% of the cycles measured. The same

happens with the set voltage (V_{SET}) and reset voltage (V_{RESET}): the value of V_{SET} is 2.52 V and $C_{V.SET}$ is 0.16, while the value of V_{RESET} is -0.49 V and $C_{V.RESET}$ is 0.3. The numerical techniques employed to extract the set and reset voltages are explained in the Supplementary Note 1.

Stochastic resonance analysis

Next, we expose the Au/Ti/h-BN/Au memristors to sequences of RVS with superimposed exponential and Gaussian noises (see Fig. 3), and statistically study how the response of the devices changes. To better understand the response of the memristors under noisy signals and evaluate the presence of SR, we vary the standard deviation (σ) of the noise sources in values ranging from 50 to 150 mV, in steps of 25 mV. In Fig. 3, it is shown the input voltage signal and the corresponding current versus time (output) for consecutive set cycles. The effect of the noise added to the original RVS signal is clear (Fig. 3a and b, in the latter case for a higher noise standard deviation (SD) (in this case the noise is assumed to be Gaussian distributed with zero mean)). The corresponding current measured is given in Fig. 3c and d; see that in addition to the external noise, the inherent RS stochasticity has to be taken into account[22]. The same data shown in Fig. 3 are plotted in Supplementary Fig. 2 versus time for comparison.

We examine if the devices switch in each cycle (i.e., when applying noisy RVS), and statistically analyze the values of R_{HRS}, R_{LRS} and the R_{HRS}/R_{LRS} ratio. We use this figure-of-merit to benchmark the effect of the noise intensity because the calculation is straightforward and intuitive, based on magnitudes that can be obtained in a quasi-static approach; in addition, considering the perspective of non-volatile memory applications, the resistance ratio shows a direct improvement in the potential for these type of applications. Figure 4a-b shows the cumulative distribution function (CDF) of the R_{HRS}/R_{LRS} ratio depending on the magnitude of exponential and Gaussian noise sources added to the RVS — CDF distributions are usually employed for SR analysis in other electron devices too[16,36].
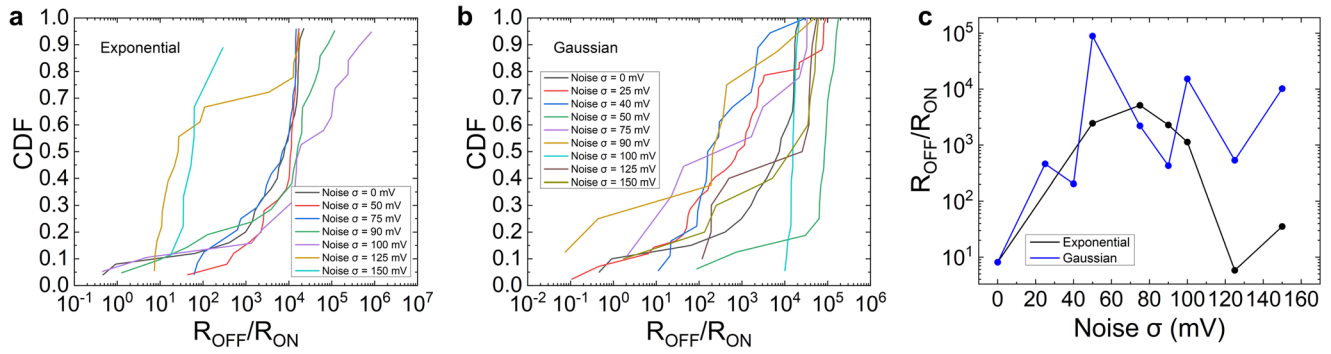
Fig. 4 Stochastic resonance description. CDFs for the R_{OFF}/R_{ON} ratio of the measured RS cycles assuming several values and types of noise, **a** exponential, **b** Gaussian. **c** Median R_{OFF}/R_{ON} ratio versus noise SD (30 values were considered for each symbol shown).
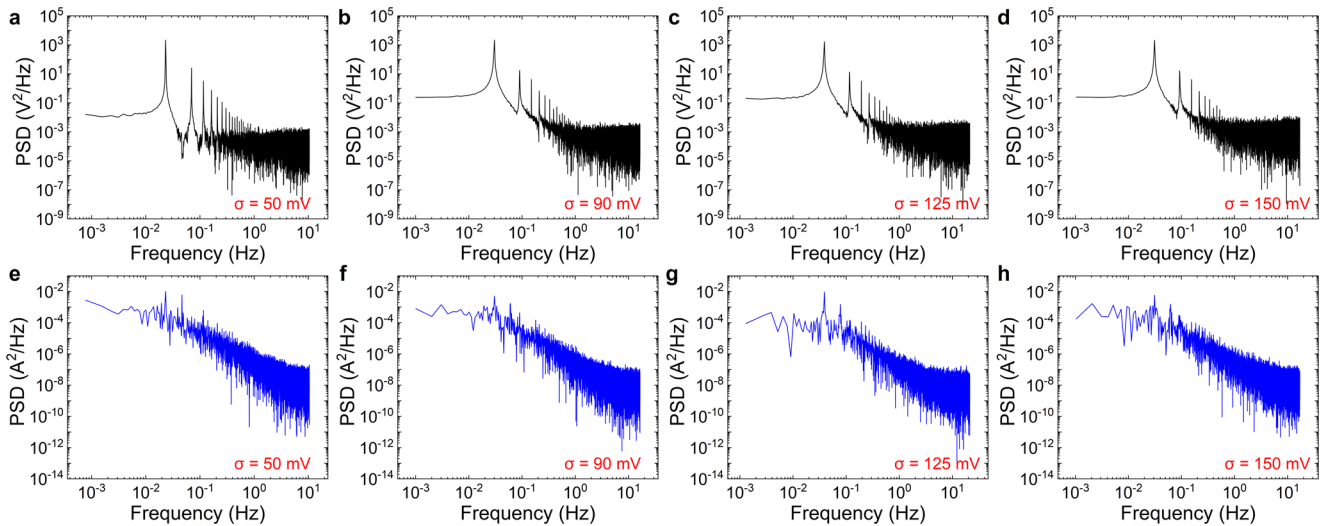

Fig. 5 Power spectrum densities. a–d Power spectrum density of the input voltage employed in the consecutive set measurements with Gaussian distributed noise for different SDs. **e–h** Current power spectrum density corresponding to the voltage data.

A higher resistance ratio can improve the device behavior in memory circuits; in this respect, it makes sense the use of the R_{OFF}/R_{ON} ratio. In addition, SR effects can also improve the resistive memory bit error rate, which is an interesting result for non-volatile memory systems[37]. The ratio of the medians of the ON and OFF resistances (due to variability, the statistical median works better than the mean in our case) versus noise SD has been plotted for the data measured in Fig. 4c. See clearly a peak for a SD of 80 mV, highlighting the existence of SR, and consequently, the constructive role of noise that can be used for memory applications. The ratio rises as the noise standard deviation increases till a SD around 80 mV is achieved. Then it drops off again for the higher SD values. This behavior is compatible with SR as it has been explained previously[11,36–38].

SR can also be studied from a formal (also in a quantitative manner) viewpoint by using the output and signal-to-noise ratio (SNR) computed from power spectral densities[39]. We have performed this analysis by using data from consecutive set processes obtained in the RS series measured. The input voltage versus time with added Gaussian distributed noise for different SDs are plotted for a few cycles in Supplementary Fig. 2 (a, b). The corresponding currents are shown in Supplementary Fig. 2 (c, d).

We have calculated the power spectral density for these magnitudes in Fig. 5, for the same SDs shown in Fig. 4. The top panels correspond to the power spectral density for the input voltage that constitutes the time series for consecutive set processes, and, in all cases, there is a clear main power peak at a

frequency $f_0 \in (0.02, 0.03) Hz$, corresponding to the inverse of the "set" phase period which is around 30–50 seconds. Secondary peaks in the power spectra density correspond to harmonics of the main peak frequency appearing at $(2n+1)f_0$ with $n = 1, 2 \ldots$; and their appearance indicates that the voltage input signals are not purely periodic. In the bottom panels similar power spectral densities are depicted for the resulting output current time series, corresponding to the voltage time series plotted above; and, although these are noisier, still the main power peak at f_0 is clearly illustrated. However, the prominence of such a main frequency peak over the background of noise frequencies f_i is not the same for all considered Gaussian noise SDs. To quantify such main peak prominence over the noise frequencies around it, the signal to noise ratio (SNR) is commonly used, defined as the ratio among the amplitude of the main frequency peak over the mean power of the surrounding noisy frequencies and the standard deviation of the power of the surrounding noise frequencies. More specifically we used the following measure for the SNR:

$$SNR = \frac{PSD(f_0) - \langle PSD(f_i) \rangle}{\sqrt{\langle PSD^2(f_i) \rangle - \langle PSD(f_i) \rangle^2}} \tag{1}$$

where $f_i \in \left(f_0 - \frac{n}{T}, f_0 + \frac{n}{T}\right), f_i \neq f_0$, being T the time duration in seconds of the voltage time series, n are the number of noise frequencies considered around the mean frequency peak and $\langle . \rangle$ is an average over these noisy frequencies f_i.
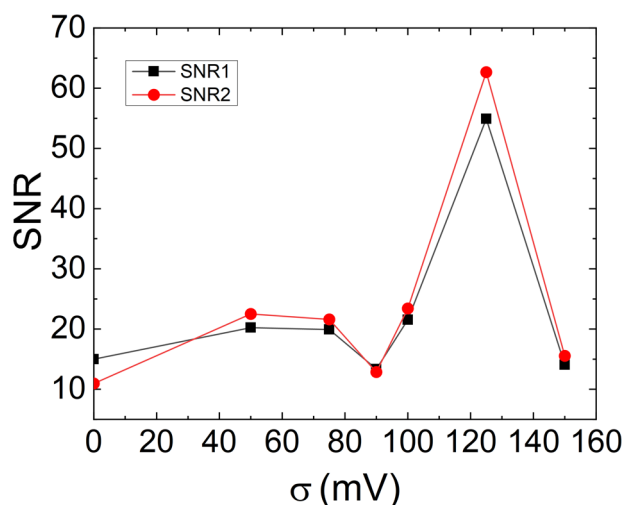
Fig. 6 Signal to noise ratio versus Gaussian distributed SD. SNR1 (SNR2) data correspond to 20 (30) noisy frequencies selected around the principal peak in the current PSD (such as those plotted in Fig. 5).

The behavior of SNR computed for the PSD of the output current time series for different noise voltage SDs is plotted in Fig. 6 for two different values of *n*. This clearly shows that there is a SNR enhancement for a noise SD value around 125 mV, depicting a SR phenomenon. Our analysis also reveals a possible secondary SNR enhancement around a noise with SD of 60 mV, and that could be related with the SR peak observed using the R_{OFF}/R_{ON} protocol (see Fig. 4c), a fact that needs further exploration. Note that our findings are robust since they remain qualitatively and quantitatively the same when one varies the number of noise frequencies used to compute the SNR.

It is important to highlight the different noise intensities at which the main resonance shows up when analyzing SR in Figs. 4 and 6. The methodology followed in Fig. 6 is the conventional SR analysis tool[11,39]. The SDs corresponding to the resonance peak are linked to an optimization of the SNR in a frequency sweep. These SDs are higher than in the case of the R_{HRS}/R_{LRS} ratio. This latter methodology is better adapted for memory applications. However, as highlighted above, the conventional SR analysis also depicts a possible lower noise and lower amplitude resonance peak around the SDs at which the R_{HRS}/R_{LRS} ratio shows its enhancement, and both peaks could be then related indicating the possibility of double SR phenomena, as it has already been reported in other systems[3,4,40].

METHODS

Device fabrication

We fabricate Au/Ti/h-BN/Au/Ti memristors with cross-point structure and lateral size of 5 μm × 5 μm using an industry-compatible process. First, we clean a 300 nm SiO_2/Si sample with acetone, isopropanol and deionized water using an ultrasonication bath for 10 minutes (each step). Then, we do photolithography (mask aligner SUSS MJB4) to pattern the bottom electrodes and deposit 10 nm Ti (first) and 40 nm Au (second) using a Kurt J. Lesker PVD75 electron beam evaporator without breaking the vacuum of 3×10^5 torr. Next, we transfer a sheet of multilayer h-BN (~6-nm-thick, or ~18 layers), previously grown by chemical vapor deposition (CVD) on Cu foil, onto the SiO_2/Si sample containing the bottom electrodes. The wet transfer method used is explained in detail in our previous publications[41,42]. Finally, top electrodes, similar to the bottom ones but rotated 90°, are patterned by photolithography and electron beam evaporator, leading to a small cross-point

Au/Ti/h-BN/Au region (the Ti underneath the bottom Au film is simply an adhesion layer and it does not play any role in the electronic properties of the devices).

Device characterization

Optical microscopy was performed using a Leica DM400 polarizing microscope. For TEM investigations, lamellae were prepared with the Helios nanolab 450 S/Helios G4 focus ion beam (FIB) system. These lamellae were subsequently transferred to TEM grids and analyzed under a JEM-2100 high-resolution TEM from FEI, operated at 200 kV. The devices were measured by means of a Keysight B1500A semiconductor parameter analyser and a probe station (Karl Suss PSM6). A B1511B medium power source measurement unit (MPSMU) was used for the quasi-static ramped voltage stress measurements. Different types of noise were implemented and added to the triangular signals employed in the characterization process.

REFERENCES

1. Benzi, R., Sutera, A. & Vulpiani, A. The mechanism of stochastic resonance. *J. Phys. A* **14**, L453 (1981).
2. Bezrukov, S. M. & Vodyanoy, I. Noise-induced enhancement of signal transduction across voltage-dependent ion channels. *Nature* **378**, 362–364 (1995).
3. Mejias, J. F. & Torres, J. J. Emergence of resonances in neural systems: the interplay between adaptive threshold and short-term synaptic plasticity. *PloS one* **6**, e17255 (2011).
4. Torres, J. J., Marro, J. & Mejias, J. F. Can intrinsic noise induce various resonant peaks? *New J. Phys.* **13**, 053014 (2011).
5. Douglass, J. et al. Noise enhancement of information transfer in crayfish mechanoreceptors by stochastic resonance. *Nature* **365**, 337–340 (1993).
6. Vaquez-Rodriguez, B. et al. Stochastic resonance at criticality in a network model of the human cortex. *Sci. Rep.* **7**, 13020 (2017).
7. Torres, J. J. & Marro, J. Brain performance versus phase transitions. *Sci. Rep.* **5**, 12216 (2015).
8. Torres, J. J. & Marro, J. Physics clues on the mind substrate and attributes. *Front. Comput. Neurosci.* **16**, 836532 (2022).
9. Russell, D. F., Wilkens, L. A. & Moss, F. Use of behavioural stochastic resonance by paddle fish for feeding. *Nature* **402**, 291 (1999).
10. Levin, J. E. & Miller, J. P. Broadband neural encoding in the cricket cereal sensory system enhanced by stochastic resonance. *Nature* **380**, 165 (1996).
11. Mikhaylov, A. N. et al. Stochastic resonance in a metal-oxide memristive device. *Chaos Solit.* **144**, 110723 (2021).
12. Fauve, S. & Heslot, F. Stochastic resonance in a bistable system. *Phys. Lett. A* **97**, 5 (1983).
13. Mantegna, R. N. & Spagnolo, B. Stochastic resonance in a tunnel diode. *Phys. Rev. E* **49**, R1792 (1994).
14. Marro, J. & Torres, J. J. Phase Transitions in Grey Matter: Brain Architecture and Mind Dynamics, AIP Publish. LLC, (2021).
15. Pinamonti, G., Marro, J. & Torres, J. J. Stochastic resonance crossovers in complex networks. *PloS one* **7**, e51170 (2012).
16. Dodda, A. & Das, S. Demonstration of stochastic resonance, population coding, and population voting using artificial MoS2 based synapses. *ACS Nano* **15**, 16172–16182 (2021).
17. Tang, J. et al. Bridging Biological and Artificial Neural Networks with Emerging Neuromorphic Devices: Fundamentals, Progress, and Challenges. *Adv. Mat.* **31**, 1902761 (2019).

18. Lanza, M. et al. Memristive technologies for data storage, computation, encryption and radio-frequency communication. *Science* **376**, 1–13 (2022).

19. von Witzleben, M. et al. Investigation of the impact of high temperatures on the switching kinetics of redox-based resistive switching cells using a high-speed nanoheater. *Adv. Elect. Mat.* **3**, 1700294 (2017).

20. Aldana, S. et al. Resistive Switching in HfO$_2$ based valence change memories, a comprehensive 3D kinetic Monte Carlo approach. *J. of Phys. D: Appl. Phys.* **53**, 225106 (2020).

21. Ielmini, D. & Waser, R. Resistive Switching: From Fundamentals of Nanoionic Redox Processes to Memristive Device Applications, Wiley-VCH, (2015).

22. Roldán, J. B. et al. Variability in resistive memories. *Adv. Intell. Syst.* **5**, 2200338 (2023).

23. Acal, C. et al. Holistic variability analysis in resistive switching memories using a two-dimensional variability coefficient. *ACS Appl. Mat. Int* **15**, 19102–19110 (2023).

24. Spiga, S., Sebastian, A., Querlioz, D. & Rajendran, B., Memristive devices for brain-inspired computing, Elsevier, (2020).

25. Roldan, J. B. et al. Modeling the variability of Au/Ti/h BN/Au memristive devices. *IEEE Trans. on Electron Devices* **70**, 1533–1539 (2022).

26. Xie, J., Afshari, S. & Sanchez Esqueda, I. Hexagonal boron nitride (h-BN) memristor arrays for analog-based machine learning hardware. *npj 2D Mat. Appl.* **6**, 50 (2022).

27. Wang, Y. et al. Energy-efficient synaptic devices based on planar structured h-BN memristor. *J. Alloys Compd.* **909**, 164775 (2022).

28. Magyari-Köpe, B.& Nishi, Y., Advances in non-volatile memory and storage technology, Woodhead Publishing Series in Electronic and Optical Materials Elsevier, (2020).

29. Shi, Y. et al. Electronic synapses made of layered two-dimensional material. *Nat. Electron.* **1**, 458–465 (2018).

30. Wedig, A. et al. Nanoscale cation motion in TaOx, HfOx and TiOx memristive systems. *Nat. Nanotechnol.* **11**, 67 (2016).

31. Pan, C. et al. Coexistence of grain-boundaries-assisted bipolar and threshold resistive switching in multilayer hexagonal boron nitride. *Adv. Funct. Mater.* **27**, 10 (2017).

32. Shen, Y. et al. Variability and Yield in h-BN-Based Memristive Circuits: The Role of Each Type of Defect. *Adv. Mat.* **33**, 2103656 (2021).

33. Hattori, Y., Taniguchi, T., Watanabe, K. & Nagashio, K. Layer-by-layer dielectric breakdown of hexagonal boron nitride. *ACS Nano* **9**, 916 (2015).

34. Lanza, M. et al. Temperature of conductive nanofilaments in hexagonal boron nitride based memristors showing threshold resistive switching, *Adv. Elect. Mat.*, 2100580, (2021).

35. Dodda, A. et al. Stochastic resonance in MoS2 photodetector. *Nat. Commun.* **11**, 4406 (2020).

36. Maldonado, D. et al. TiN/Ti/HfO$_2$/TiN memristive devices for neuromorphic computing: from synaptic plasticity to stochastic resonance. *Front. in Neurosci.* **17**, 1271956 (2023).

37. Ntinas, V. et al. Power-Efficient Noise-Induced Reduction of ReRAM Cell's Temporal Variability Effects, in IEEE Trans. *Circuits and Syst. II: Express Briefs* **68**, 1378–1382 (2021).

38. McDonnell, M. D., Stocks, N. G., Pearce, C. E. M. & Abbott, D. Stochastic resonance, Cambridge University Press (New York), (2008).

39. Gammaitoni, L., Hänggi, P., Jung, P. & Marchesoni, F. Stochastic resonance. *Rev. Mod. Phys.* **70**, 223–287 (1998).

40. Palabas, T., Torres, J. J., Perc, M. & Uzuntarla, M. Double stochastic resonance in neuronal dynamics due to astrocytes. *Chaos, Solit* **168**, 113140 (2023).

41. Zhu, K. et al. Hybrid 2D/CMOS microchips for memristive applications. *Nature* **618**, 57–62 (2023).

42. Zhu, K. et al. The development of integrated circuits based on two-dimensional materials. *Nat. Electron.* **4**, 775–785 (2021).

AUTHOR CONTRIBUTIONS

Conceptualization by J.B.R. and M.L.; electrical measurements, data curation and modeling by D.M., A.C. and J.J.T.; Y.S., W.Z., Y.Y. fabricated the h-BN memristors. The original draft preparation, review and editing by J.B.R., M.L., D.M., J.J.T. All coauthors have checked and validated the final version of the manuscript.

COMPETING INTERESTS

The authors declare no competing interests.

ADDITIONAL INFORMATION

Supplementary information The online version contains supplementary material available at https://doi.org/10.1038/s41699-024-00444-1.

Correspondence and requests for materials should be addressed to J. B. Roldán or M. Lanza .

Reprints and permission information is available at http://www.nature.com/reprints

Publisher's note Springer Nature remains neutral with regard to jurisdictional claims in published maps and institutional affiliations.